

# Nanoparticle-modified electrodes

Stephen R. Belding, Fallyn W. Campbell, Edmund J. F. Dickinson and Richard G. Compton\*

Received 15th April 2010, Accepted 14th June 2010

DOI: 10.1039/c0cp00233j

The behaviour of nanoparticle-modified electrodes is compared and contrasted with that of conventional unmodified macroelectrodes.

## 1. Introduction

Metals in the form of nanoparticles can show qualitatively different behaviour from that of the bulk material.<sup>1</sup> Perhaps the most clear-cut example of this is that of gold: whereas bulk gold is a relatively non-reactive metal, as nanocrystals of a few hundred atoms it becomes highly active catalytically, for example in respect of selective oxidation reactions such as alkene epoxidation or alcohol oxidation and the synthesis of hydrogen peroxide from hydrogenation of di-oxygen.<sup>2,3</sup>

Bulk metals are, of course, widely deployed as electrode materials to facilitate a variety of electrolytic processes. The latter range from the synthetic (aluminium, chlorine, and nylon synthesis) through the analytical (sensors for smoke detection *via* carbon monoxide in air, or for glucose in blood to facilitate the regulation of diabetes) to the energy storage/production areas of fuel cells, batteries, solar cells *etc.*

The range of metallic materials used in electrochemistry is wide and diverse; that said, the properties of electrodes for selected tasks have been improved and optimised by means of their 'chemical modification'.<sup>4,5</sup> That is, by immobilising molecules, polymers, films, *etc.* on the surface of conventional electrode materials, their properties can be changed notably,

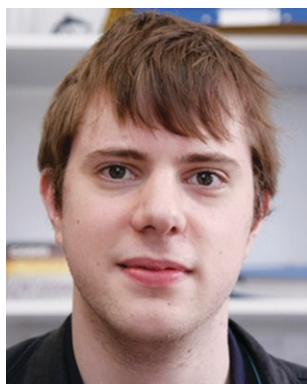
for example in respect to the electron transfer kinetics for various selected target species. Recently<sup>6</sup> electrode surfaces have been modified by growing or casting 'arrays' of nanoparticles onto their surface. Providing then that the nanoparticles are in electrical contact with the substrate electrode, each nanoparticle can act as a tiny electrode, so that the electrode surface has the electrochemical properties of the nanoparticle material rather than (or strictly as well as) that of the supporting electrode. Typically, the latter might be carbon-based for reasons of cost effectiveness, but a wide range of other supports have been used.<sup>6</sup> Fig. 1 shows the growth of cobalt nanoparticles on the surface of a boron-doped diamond electrode<sup>7</sup> as imaged by electrochemical atomic force microscopy; in these experiments the cobalt nanoparticles are grown *via* electrodeposition. In contrast Fig. 2 shows scanning electron microscopy (SEM) images of silver nanoparticles which, for analytical purposes, can be cast onto an electrode made of basal plane pyrolytic graphite.<sup>8</sup>

The purpose of this paper is to consider the behaviour of nanoparticle-modified electrodes and to ask in what ways this can differ from that of conventional unmodified macroscale electrodes.

## 2. Types of electrode reaction

The general reader will be familiar with the concepts of outer sphere and inner sphere electron transfer as pertain to electron transfer between two molecules in homogeneous solution.<sup>9</sup> In heterogeneous electron transfer, analogous

Department of Chemistry, Physical and Theoretical Chemistry Laboratory, Oxford University, South Parks Road, Oxford, OX1 3QZ, United Kingdom. E-mail: richard.compton@chem.ox.ac.uk; Fax: +44 (0) 1865 275410; Tel: +44 (0) 1865 275413



Stephen R. Belding

Stephen R. Belding received an MChem degree from the University of Oxford in 2009. He is currently studying for a DPhil under the supervision of Richard G. Compton, at the same university. His interests include the theoretical study of voltammetric processes at nanoparticles.



Fallyn W. Campbell

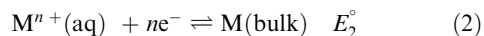
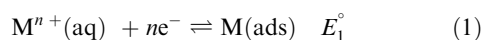
Fallyn W. Campbell received a BSc degree in chemistry from the University of Edinburgh in 2007. She is currently studying for a DPhil under the supervision of Richard G. Compton at the University of Oxford. Her interests include the experimental study of electrochemical processes at nanoparticles.

kinetic cases are also seen, with the outer sphere case corresponding to the reactant being located at the Outer Helmholtz Plane, corresponding to the distance of closest approach to the electrode such that the layer of solvent molecules adsorbed on the electrode surface is not penetrated by the reactant or its coordination sphere.<sup>10</sup> In contrast, the inner sphere limit corresponds to specific adsorption of the reactant on the electrode surface.

It is evident that the latter type of electrode process is likely to show differences between the macro- and nanoscales, since adsorption will be sensitive to the surface structure: both electronic and topological. The next section considers examples of such differences before we make the same comparison for outer sphere type electrode processes.

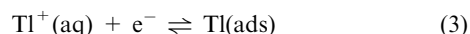
### 3. Electrode reactions involving adsorption

A first example of altered electrochemical behaviour between the nano- and macroscales concerns the phenomenon of underpotential deposition (upd). This is the electrodeposition of a monolayer, or sub-monolayer, of one metal onto a different (substrate) metal at potentials more positive (less negative) than those required for the bulk deposition:



where  $E_1^\circ > E_2^\circ$ .

The upd of thallium on silver macroelectrodes has been studied using both polycrystalline and single-crystal electrodes:



The structure of the surface sensitively influenced the ease with which the metal could be deposited:  $\text{Ag}(111) > \text{Ag}(100) > \text{Ag}(110) > \text{polycrystalline Ag}$ .<sup>11,12</sup> These observations encouraged

a study of the corresponding phenomenon on silver nanoparticles (AgNPs) of varying sizes<sup>13</sup> which were synthesised by a seed-mediated citrate reduction process with the formation of AgNPs with the following diameters: 20–40 nm, 50–70 nm and 80–120 nm. The resulting colloidal AgNPs suspensions were cast on the surface of a basal plane pyrolytic graphite electrode (BPPG).

Thallium upd was first carried out on a macrodisc electrode (diameter 0.7 cm) using a solution of 10 mM  $\text{TlNO}_3$  in 1.5 M  $\text{KNO}_3$ . Fig. 3 shows the resulting voltammetry with underpotential deposition with a peak potential of  $-0.545$  V vs. the saturated calomel electrode (SCE) and corresponding stripping at  $-0.440$  V. The bulk deposition of thallium is apparent at more negative potentials, together with a bulk stripping peak on the positive direction sweep of the voltammogram. Comparison of this behaviour with differently sized AgNPs on BPPG showed the responses shown in Fig. 4 and 5. In all cases bulk deposition is seen but the thallium upd is only apparent for the nanoparticles of 80–120 nm diameter and is not observed for the 20–40 nm sized particles. The results show that qualitatively different adsorption behaviour is seen with a size threshold of *ca.* 50 nm with thallium adsorption absent below. Such behaviour in other systems can, of course, explain differences in electrode reaction mechanisms between the macro- or micro- and the nanoscales. Analogous observations have been made for the upd of lead and cadmium on AgNPs.<sup>14</sup> Similarly the upd of thallium has been studied in respect of gold nanoparticles (AuNPs) supported on multiwalled carbon nanotubes (MWCNTs), as shown in Fig. 6.<sup>15</sup> The upd deposition and study of thallium was observed on macro-gold and on large nanoparticles (30–60 nm diameter) but was completely absent on the 10 nm diameter sized gold nanoparticles despite the fact that the nanoparticles were shown to be in electrical contact with the nanotubes and the supporting electrode.

As a second illustration of altered adsorption between the macro- and nanoscales, we consider the reduction of hydrogen peroxide at silver electrodes under acidic conditions. For polycrystalline macroelectrodes the work of Ertl<sup>16</sup>



Edmund J. F. Dickinson

*Edmund J. F. Dickinson received an MChem degree from the University of Oxford in 2008. He is currently studying for a DPhil under the supervision of Richard G. Compton, at the same university. His interests include the theoretical study of interfacial processes at nanoparticles.*



Richard G. Compton

*Richard G. Compton is a professor of chemistry at the University of Oxford and a tutorial fellow at St John's College. He is the editor in chief of the Elsevier journal, Electrochemistry Communications, and is a scientific founder of a spin-out company, OxTox Limited. He has published over 950 articles in refereed journals and has an h-index of 59 (as of June 2010). In addition, he has authored several undergraduate textbooks, including Understanding Voltammetry (World Scientific, 2nd edition, 2010).*

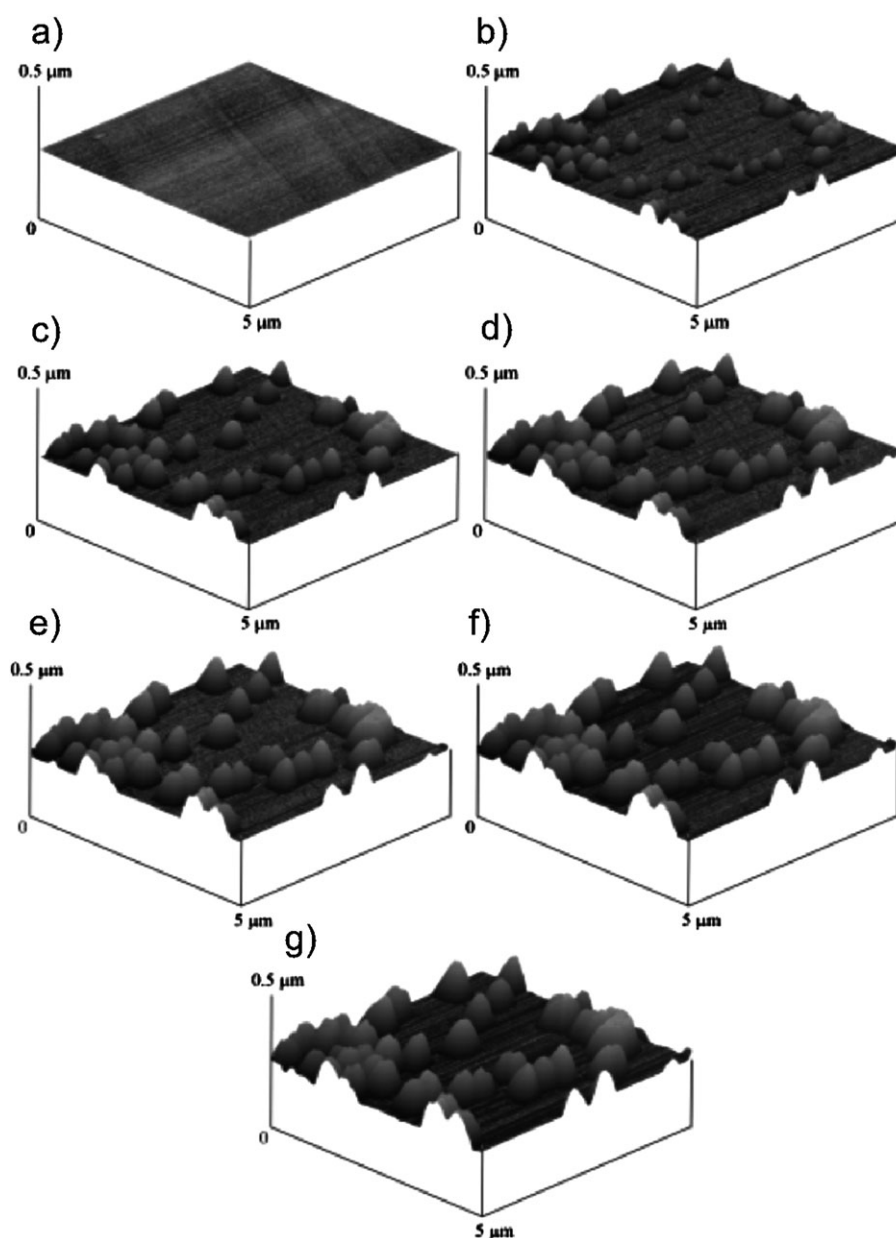


**Fig. 1** *In situ* electrochemical atomic force microscopy of cobalt nuclei growth, deposited onto boron-doped diamond from a 10 mM  $\text{Co(II)}$  solution at  $-1.15$  V vs. SCE for (a)–(g) 0, 10, 20, 30, 40, 50, and 60 s respectively. Reproduced from ref. 7 with permission, © Wiley-VCH 2006.

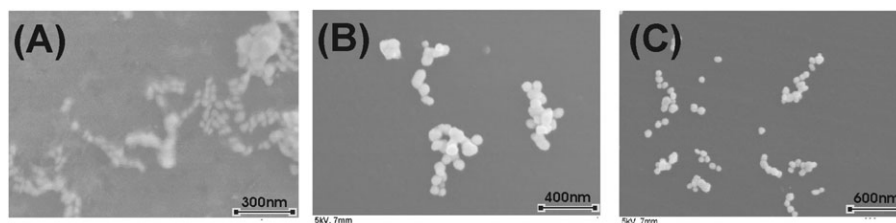


**Fig. 2** SEM images of colloidal citrate-capped AgNPs: (A) 20–40 nm, (B) 50–70 nm, and (C) 80–120 nm. SEM carried out on a carbon film/copper grid substrate. Reproduced from ref. 8 with permission, © American Chemical Society 2009.

has shown that two parallel mechanisms operate: first the ‘normal’ reduction (at potentials more negative than

$-0.4$  V vs.  $\text{Hg}/\text{Hg}_2\text{SO}_4$ ) with a transfer coefficient,  $\alpha$ ,  $\approx 0.23$ , and an ‘activated’ mechanism seen at a less negative

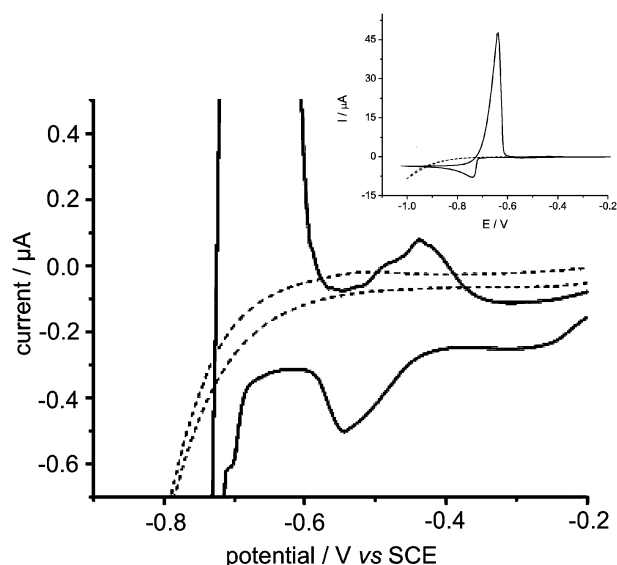


**Fig. 3** Thallium deposition on a silver macrodisc electrode. Experimental conditions:  $\text{KNO}_3$  (1.5 M) +  $\text{TINO}_3$  vs. SCE. Scan rate:  $50 \text{ mV s}^{-1}$ . (Solid line: 10 mM  $\text{TINO}_3$ ; dashed line: 0 mM  $\text{TINO}_3$ ). Reproduced from ref. 13 with permission, © Royal Society of Chemistry and the Centre National de la Recherche Scientifique 2010.

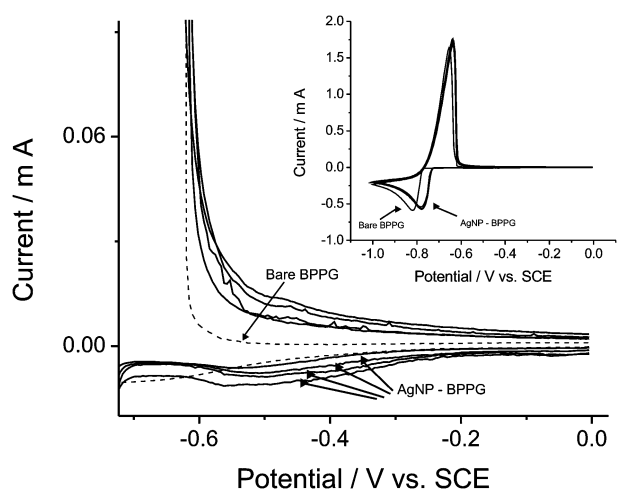
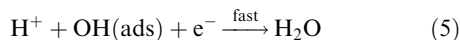
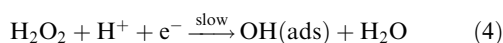


**Fig. 4** Thallium deposition on a AgNP-BPPG (2040 nm) electrode. Experimental conditions:  $\text{KNO}_3$  (1.5 M) +  $\text{TINO}_3$  vs. SCE. Scan rate:  $50 \text{ mV s}^{-1}$ . (Solid line: AgNP-BPPG (2040 nm) electrode; dashed line: bare BPPG). Reproduced from ref. 13 with permission, © Royal Society of Chemistry and the Centre National de la Recherche Scientifique 2010.

potential ( $-0.1 \text{ V vs. Hg/Hg}_2\text{SO}_4$ ,  $\alpha \approx 0.40$ ). The mechanism of the normal reduction is thought to be:



The normal reduction provides an initial source of  $\text{OH(ads)}$  which allows the activated process to occur at a faster rate *via* the following mechanism:

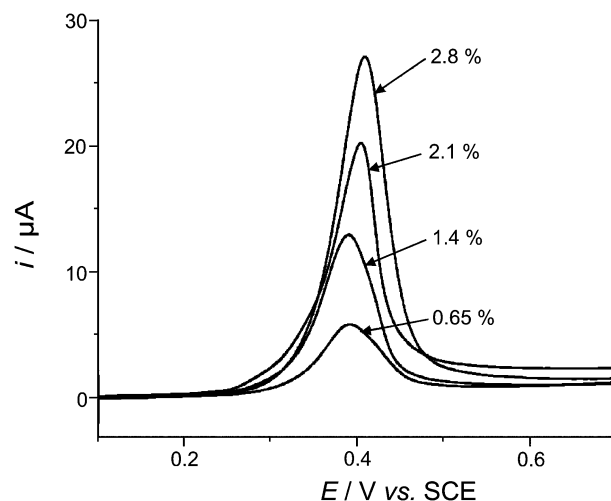
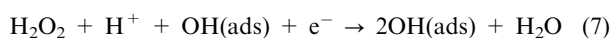
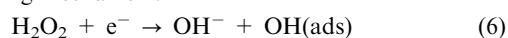


**Fig. 5** Stripping voltammograms recorded for increasing surface coverage of AgNPs (2040 nm, 0.5 and 3.0%). Experimental conditions:  $\text{NaClO}_4$  (0.1 M) vs. SCE. Scan rate:  $20 \text{ mV s}^{-1}$ . Reproduced from ref. 13 with permission, © Royal Society of Chemistry and the Centre National de la Recherche Scientifique 2010.

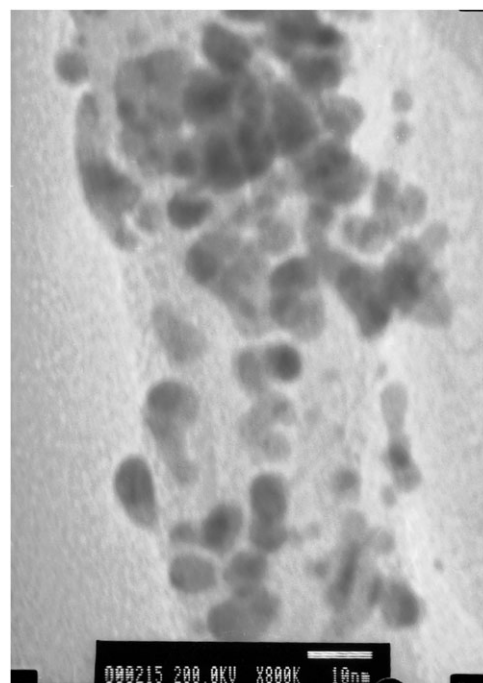


**Fig. 6** A transmission electron microscopy (TEM) image showing the gold nanoparticles encrusting a bamboo-like MWCNT. Reproduced from ref. 15 with permission, © Royal Society of Chemistry and the Centre National de la Recherche Scientifique 2010.

The mechanism is 'autocatalytic' as the presence of adsorbed  $\text{OH}$  increases the rate of the above process and results in further  $\text{OH}$  adsorption on the silver surface. Fig. 7 shows the voltammetry associated with the two processes. Fig. 8 shows the voltammetry at a AgNP-modified electrode. In contrast to the macroelectrode behaviour, the autocatalytic process was entirely absent under all conditions studied, testifying to the altered adsorption behaviour at the nanoscale.



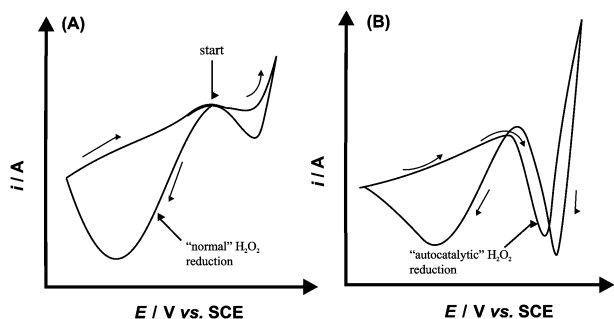


**Fig. 7** Schematic representation of voltammetry at a stationary Ag electrode in an electrolyte of 0.1 M HClO<sub>4</sub> + 20 mM H<sub>2</sub>O<sub>2</sub>, with a scan rate of 100 mV s<sup>-1</sup>. (A) First scan, beginning at the start point and sweeping the potential first in a positive direction. Only normal H<sub>2</sub>O<sub>2</sub> reduction can be observed in the reverse sweep. (B) Subsequent scans displaying an autocatalytic reduction peak at more positive potential as well as the normal reduction at a higher overpotential. Reproduced from ref. 8 with permission, © American Chemical Society 2009.

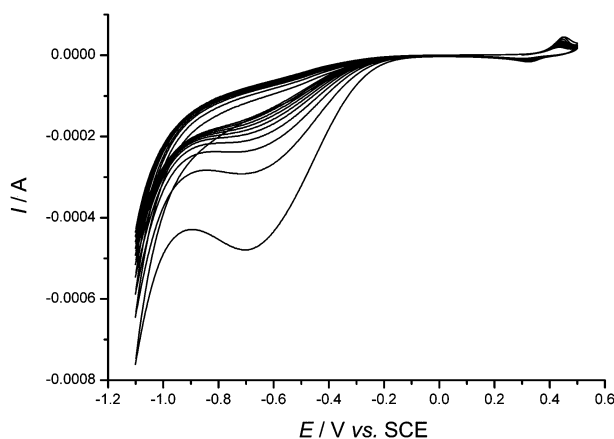


**Fig. 8** Reduction of H<sub>2</sub>O<sub>2</sub> at a AgNP-modified electrode: autocatalytic reduction absent in the voltammetry. Data is shown for a high nanoparticle surface coverage. Reproduced from ref. 8 with permission, © American Chemical Society 2009.

Fig. 9 and 10 show further data for the H<sub>2</sub>O<sub>2</sub>/AgNP system. First, when the AgNP coverage is such that the nanoparticles are diffusionally isolated then the peak potential for the reduction wave varies with the particle size ( $r_{np}$ ) as shown in Fig. 9, with the reduction moving to more negative values as the radius shrinks. Second, as shown in Fig. 10, the peak potential is sensitive to the coverage of nanoparticles on the electrode; as the coverage increases, the peak potential for the reduction moves to more positive (less negative) potentials.

The dependence of the peak potential on both the radius and the coverage reflects both the rate of the electrolytic process and that of the mass transport to and from the nanoparticles. In the case of the data shown in Fig. 10 and 11, the size of the nanoparticles is sufficiently large and the concentration of supporting electrolyte sufficiently high that a diffusion-only approach to transport can be usefully adopted, as discussed in the next section.

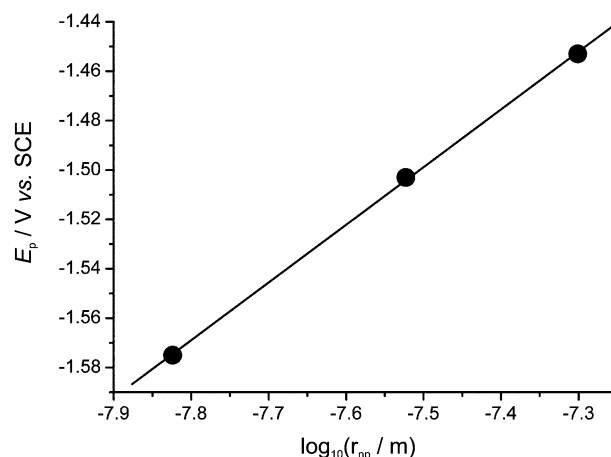


**Fig. 9** Reduction of H<sub>2</sub>O<sub>2</sub> at a AgNP-modified electrode:  $E_p$  vs.  $\log(r_{np})$  for isolated nanoparticles;  $\alpha = 0.253$ . Reproduced from ref. 8 with permission, © American Chemical Society 2009.

## 4. Electrolysis at large nanoparticles and their arrays

### 4.1 Isolated nanoparticles

For sufficiently large and diffusionally isolated nanoparticles supported on a planar electrode, a diffusion-only model can provide useful insight into the expected current–voltage behaviour, assuming the electrolysis is confined to the surface of the nanoparticle with none occurring on the electrode support. The approach is likely to be quantitative for nanoparticles larger than *ca.* 10 nm in size, provided the electrolysis is conducted in the presence of a sufficiently large concentration of supporting electrolyte. Fig. 11 schematically shows (well separated) nanoparticles on an electrode with identical spherical and hemispherical shapes; Fig. 12 shows coordinate systems used to describe these isolated nanoparticles.

The current–voltage response at the isolated nanoparticles will depend on the voltage scan rates (V s<sup>-1</sup>). However, for suitably slow scan rates a diffusion limited current,  $i_{lim}$ , will be established. For a hemispherical electrode:

$$i_{lim} = 2\pi nFD_A r_{np}[A]_{bulk} \quad (8)$$

where  $r$  is the radius for the nanoparticle and  $D_A$  is the diffusion coefficient of the electroactive species A, which undergoes the following electrocatalytic process at the surface of the hemispherical nanoparticles:

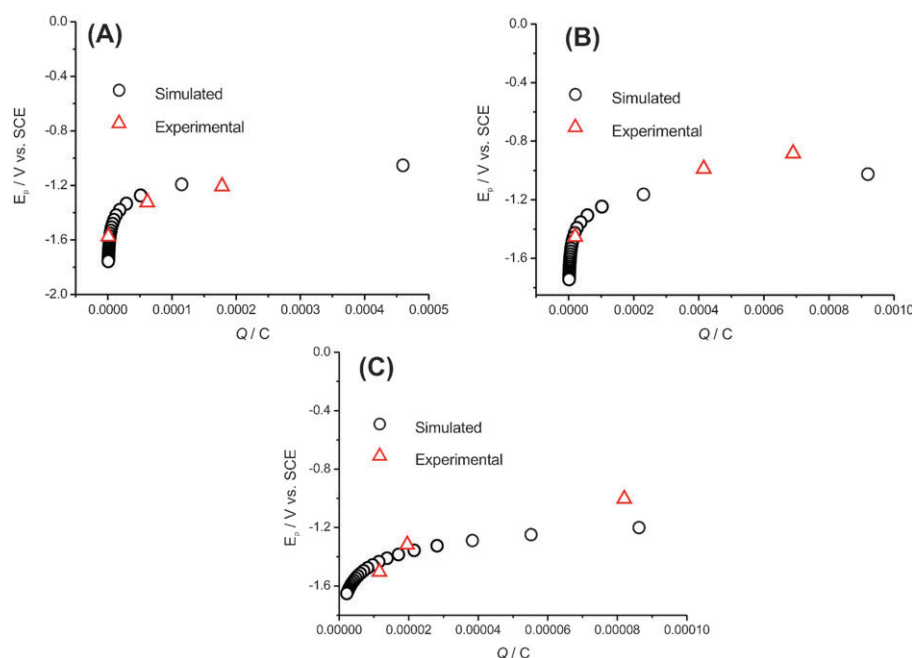


$F$  is the Faraday constant and  $[A]_{bulk}$  is the bulk concentration of A. For the case of a sphere,

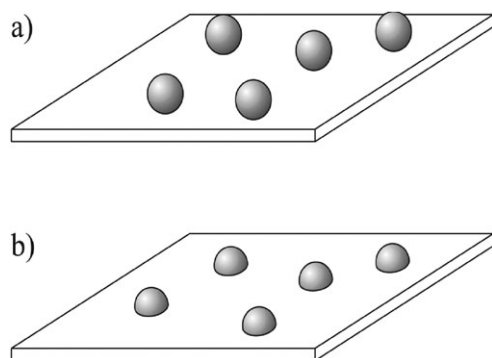
$$i_{lim} = 8.71nFD_A r_{np}[A]_{bulk} \quad (10)$$

Fig. 13 shows the concentration profile of A surrounding the nanoparticle under these conditions ( $R = \frac{r}{r_{np}}$  and  $Z = \frac{z}{r_{np}}$ ). For an isolated sphere in free solution,  $i_{lim}$  is given by equation:

$$i_{lim} = 4\pi nFD_A r_{np}[A]_{bulk} \quad (11)$$



**Fig. 10** Plot of peak potential,  $E_p$ , calculated for  $\text{H}_2\text{O}_2$  reduction at an array of AgNPs and those obtained experimentally against charge passed in Ag deposition ( $Q/C$ ), representing the coverage of NPs on the electrode surface. Data plotted for three sizes of NPs with varying degrees of NP coverage: (A)  $r_{\text{np}} = 15$  nm, (B)  $r_{\text{np}} = 30$  nm, and (C)  $r_{\text{np}} = 50$  nm. Reproduced from ref. 8 with permission, © American Chemical Society 2009.



**Fig. 11** Well-separated nanoparticles on an electrode: (a) spherical, (b) hemispherical. Reproduced from ref. 17 with permission, © American Chemical Society 2007.

Analogous expression for spheroids and hemispheroids<sup>17</sup> have been reported. Note that the limiting current for a free sphere (eqn (11)) and a sphere attached to a surface (eqn (10)) are not equal. This discrepancy is derived from the ‘shielding effect’ caused by the substrate that reduces the limiting current in the latter situation.

For fast voltage scan rates, peak shaped responses are seen. It is helpful to define a dimensionless scan rate:

$$\sigma = \left( \frac{F}{RT} \right) \left( \frac{r_{\text{np}}^2}{D_A} \right) \nu \quad (12)$$

where  $\nu$  is the true scan rate ( $\text{V s}^{-1}$ ),  $R$  is the universal gas constant and  $T$  is the absolute temperature. Fig. 15 shows the simulated voltammetry at a spherical nanoparticle for scan rates of  $\sigma = 10^{-3}$ ,  $\sigma = 1$  and  $\sigma = 10^3$ . The emergence of peak-shaped behaviour at faster scan rates is evident. Fig. 14 shows

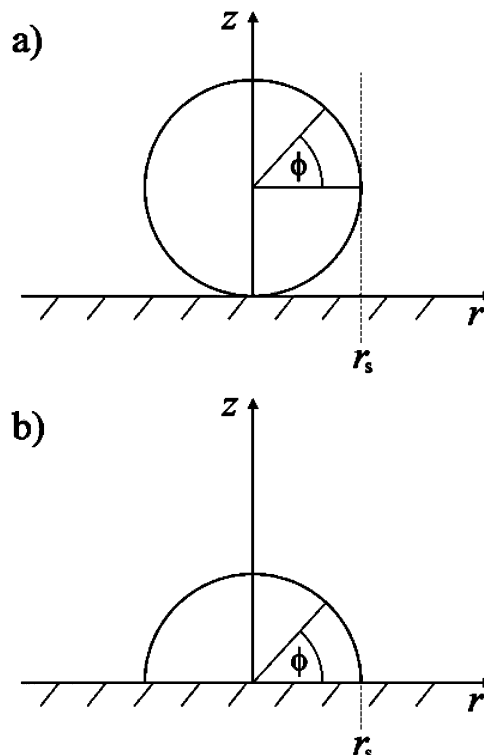


**Fig. 12** Schematic diagram of (a) a spherical particle and (b) a hemispherical particle sitting upon a supporting planar surface. Reproduced from ref. 17 with permission, © American Chemical Society 2007.

the concentration profiles of A at the potential corresponding to the peak current. It can be seen that the layer of depletion of A (the ‘diffusion layer’) shrinks as  $\sigma$  increases to the point that,

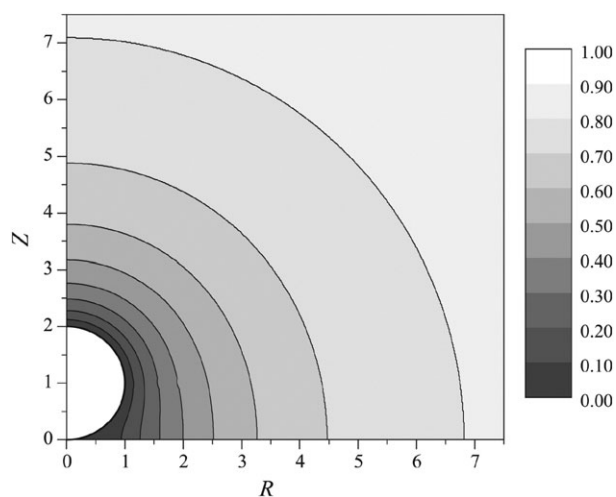


**Fig. 13** Simulated concentration profile at the spherical particle under diffusion-limiting conditions. Reproduced from ref. 17 with permission, © American Chemical Society 2007.

for  $\sigma = 10^3$ , it is confined to a very thin layer adjacent to the nanoparticle surface. The peak current changes from a scan

rate independent value at low scan rates to one which apparently scales with  $\sqrt{\sigma}$  at very fast scan rates. This reflects the change, implicit in Fig. 14, from convergent to linear diffusion. The voltammograms shown in Fig. 15 were calculated for fast ('reversible') electrode kinetics. In the corresponding slow electrode kinetics limit we would expect:

$$\frac{\partial E_p}{\partial \ln(r_{np})} = \frac{2.3RT}{(n' + \alpha)F} \quad (13)$$

where  $\alpha$  is the transfer coefficient in the electrode process and  $n'$  is the number of electrons transferred before the rate determining step. This is an important equation since it shows that the peak potential, for slow electrode kinetics, is radius dependent.

The reason for the nanoparticle size dependence of the peak potential is that this quantity reflects a switchover between rate-determining electrode kinetics, which control the current before the peak potential, to rate determining mass transport (diffusion) after the peak potential. Thus, for a fixed rate of transport, the faster the electrode kinetics, the lower the peak potential, and this is the key observation required to identify 'electrocatalysis'. Note therefore that it is not the magnitude of

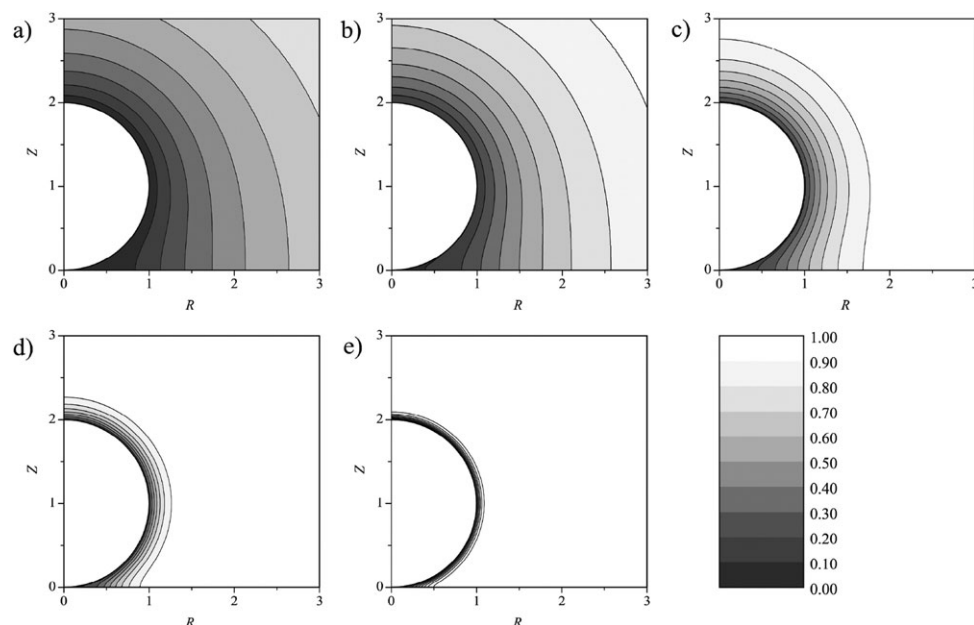


**Fig. 14** Simulated concentration profiles at the spherical particle: (a)  $\sigma = 0.1$ , (b)  $\sigma = 1$ , (c)  $\sigma = 10$ , (d)  $\sigma = 100$ , (e)  $\sigma = 1000$ . Reproduced from ref. 17 with permission, © American Chemical Society 2007.

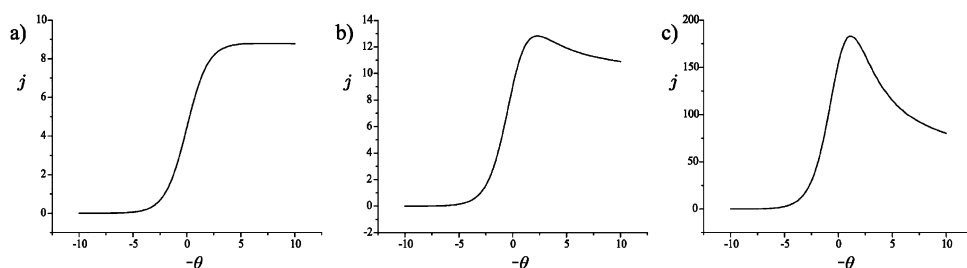


**Fig. 15** Simulated voltammetry for a reversible electrode transfer at the spherical particle. The following scan rates are used: (a)  $\sigma = 10^{-3}$ , (b)  $\sigma = 1$ , (c)  $\sigma = 1000$ . Reproduced from ref. 17 with permission, © American Chemical Society 2007.

the current but rather the value of  $E_p$  which is the key diagnostic for changes in electrode kinetics.

If the same processes are considered at electrodes of decreasing size, for example, Fig. 9 showing the variation of  $E_p$  with radius for the reduction of  $\text{H}_2\text{O}_2$  at isolated AgNPs, then the rate of mass transport increases as the size shrinks, and so for the same electrode kinetics the peak potential will occur at increasingly high potentials (more positive for an oxidation, more negative for a reduction).

It follows from the above that for an electrochemically reversible process, the peak potential will appear on nanoparticles with an *apparently* larger overpotential than at the corresponding macroelectrode and that the smaller the nanoparticle size then the greater the apparent overpotential. Both of these features are apparent in the  $\text{H}_2\text{O}_2$  reduction at silver described above. Comparison of Fig. 7 and 10 shows that large overpotentials are seen on the nanoscale as opposed to the macroscale and Fig. 9 shows that  $E_p$  becomes increasingly negative as the radius of the nanoparticle shrinks.

## 4.2 Nanoparticle arrays

A nanoparticle array is an assembly of nanoparticles supported on a conductive substrate. As with the isolated case, electrolysis is assumed to occur solely on the surface of the nanoparticles and not the underlying substrate.

Nanoparticle arrays can be synthesised in a wide variety of ways and were reviewed by Campbell *et al.*<sup>6</sup> The surface coverage of the nanoparticles is defined in terms of the area obscured in a top down view of the substrate. The relationship between the nanoparticle radius ( $r_{\text{np}}$ ), the nanoparticle separation  $\langle r_{\text{sep}} \rangle$  and the fractional surface coverage ( $\Theta$ ) is given by:

$$\Theta = \left( \frac{r_{\text{np}}}{\langle r_{\text{sep}} \rangle} \right)^2 \quad (14)$$

The electrode kinetics observed at a given nanoparticle are independent of the others in the array and therefore conform with the discussion in Section 6 below. In contrast, mass transport towards an array is substantially different than that to an isolated nanoparticle. Mass transport to a random array can be understood in terms analogous, but complementary, to those for partially blocked electrodes<sup>18,19</sup> and microdisc electrodes<sup>20–23</sup> and is based on the interaction between diffusional layers as a function of the experimental timescale and of the surface coverage. This is discussed with respect to a reversible 1 electron oxidation:

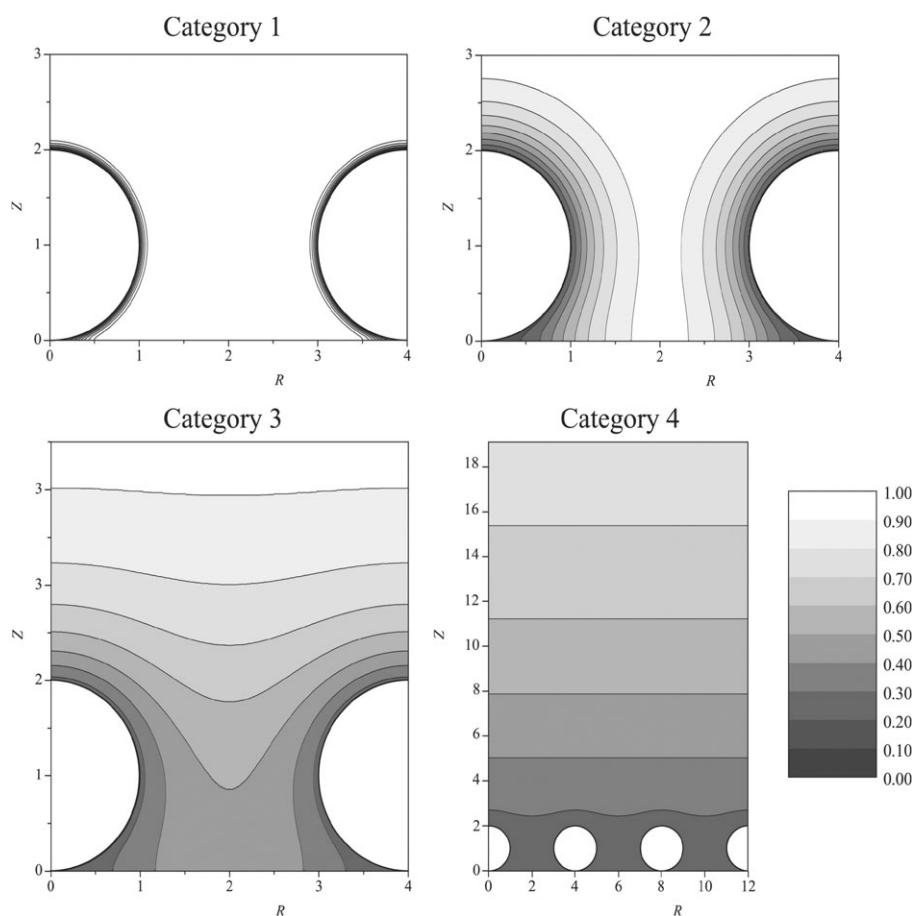


**Fig. 16** Simulated concentration profiles at a diffusion domain containing a spherical particle. Category 1:  $\sigma = 1000$ . Category 2:  $\sigma = 10$ . Category 3:  $\sigma = 1$ . Category 4:  $\sigma = 0.01$ . For all categories  $R_{\text{sep}} = \frac{r_{\text{sep}}}{r_{\text{np}}} = 2$ . Concentration profiles were taken at the linear sweep peak potential. Reproduced from ref. 50 with permission, © American Chemical Society 2007.



As the experimental timescale increases and the nanoparticle surface coverage decreases, the diffusional interaction changes from category 1 through to category 4 as shown in Fig. 16. In category 1, the diffusion layers are small and each nanoparticle is diffusionally isolated: mass transport is 1 dimensional and linear. Cyclic voltammograms in this category are peak shaped and obey the Randles–Ševčík equation ( $i_{\text{peak}} \propto \sqrt{\sigma}$ ); the chronoamperometry obeys the Cottrell equation ( $i \propto \frac{1}{\sqrt{t}}$ ). In category 2, the diffusion layers are large and approximately hemispherical but diffusional isolation between nanoparticles is maintained. The corresponding cyclic voltammograms are in steady-state with a limiting current given by eqn (10). In category 3, the depletion layers overlap and are relatively small compared to the nanoparticle separation. The cyclic voltammetry is peak shaped and the absolute current is smaller than that given by eqn (10). In category 4, the diffusion layers overlap and are relatively large compared to the nanoparticle separation. Mass transport is effectively one dimensional and linear over the entire array. As with category 1, cyclic voltammograms in this category are peak shaped and obey the Randles–Ševčík equation while the chronoamperometry obeys the Cottrell equation. The current response is similar to that obtained had the entire substrate been electroactive. This latter property is useful in catalysis as, in the category 4 region, a nanoparticle array yields a similar amount of electrolytic depletion to a macroelectrode of the same total area. This property is of practical importance as minimal amounts of expensive catalyst, such as platinum or gold, can be used to offer a maximal electrochemical response. Fig. 16 shows concentration profiles corresponding to each category for which  $R_{\text{sep}} = \frac{r_{\text{sep}}}{r_{\text{np}}} = 2$ . Note the change in scale required to resolve the increase in diffusion layer size from category 1 to category 4.

Fig. 17 shows linear sweep voltammetry for a fixed dimensionless scan rate ( $\sigma = 0.01$ ) and variable fractional surface coverage ( $\Theta$ ). The axes are given in terms of the dimensionless current per nanoparticle ( $j = \frac{i}{ND_A r_{\text{np}} F c_A}$ ). When the fractional surface coverage is very small ( $\Theta = 10^{-4}$ ), the nanoparticles are diffusionally isolated and the voltammetry is necessarily in

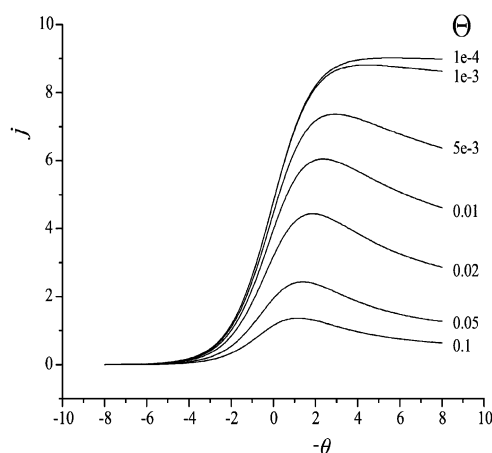


**Fig. 17** Simulated linear sweep voltammetry of a reversible electron transfer at a spherical particle modified electrode. Scan rate  $\sigma = 0.01$ ,  $\Theta$  varies from  $10^{-4}$  to 0.1. Reproduced from ref. 50 with permission, © American Chemical Society 2007.

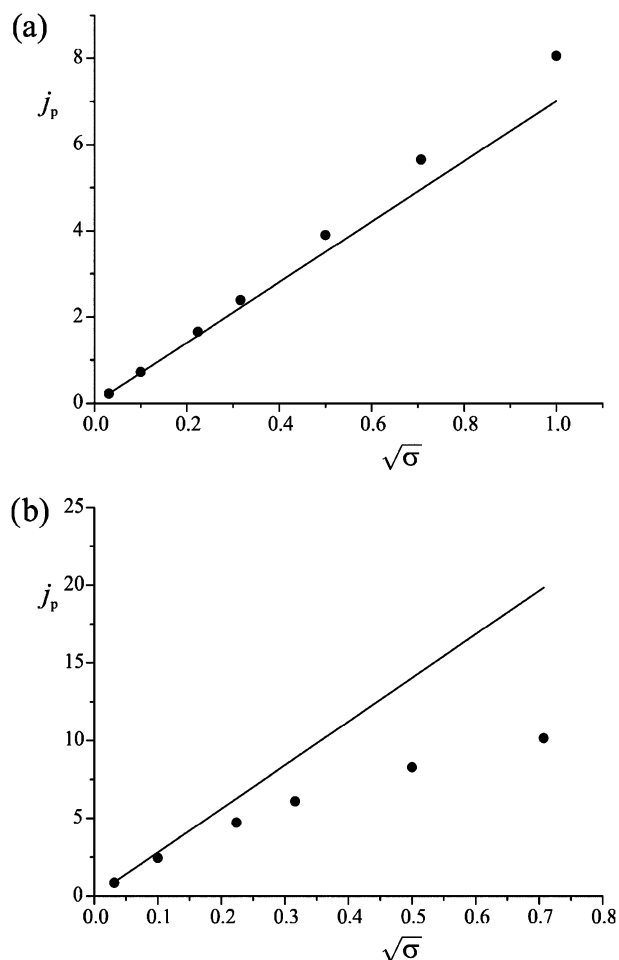


**Fig. 18** Peak current,  $j_p$ , vs. square root of the scan rate,  $\sqrt{\sigma}$ . Simulated data is shown by circles, the solid line the shows Randles–Ševčík values for planar diffusion. (a)  $\Theta = 0.2$  and (b)  $\Theta = 0.05$ . Reproduced from ref. 50 with permission, © American Chemical Society 2007.

category 1 or 2. In this situation, the experimental timescale is long enough for category 2 (steady-state) behaviour to be observed. As the fractional surface coverage is increased, the nanoparticle separation decreases and the voltammetric response passes through category 3 until eventually reaching category 4. Note that, as the surface coverage increases, the absolute size of the dimensionless current per nanoparticle decreases since the region of solution available to each nanoparticle is less.

Fig. 18 shows the dimensionless peak current ( $j_p$ ) as a function of  $\sqrt{\sigma}$  for two fractional surface coverages. In each diagram the solid line plots the Randles–Ševčík equation ( $j_p \propto \sqrt{\sigma}$ ). Category 4 behaviour can be observed at the low scan rates where overlapping of the diffusion layers is greatest. With a surface coverage of  $\Theta = 0.05$ , the peak current is smaller than the planar diffusion peak current at higher scan rates. This indicates incomplete overlapping of diffusion layers and a transition into category 3 diffusional behaviour. With a surface coverage of  $\sigma = 0.2$ , the peak current is larger than the simulated peak current from the planar diffusion value at higher scan rates. The spherical particles considered here are able to draw a higher current because their height above the

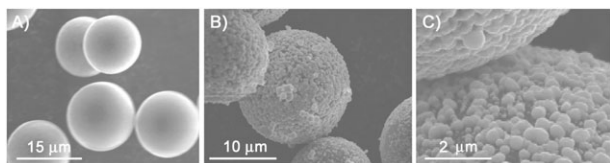


**Fig. 19** SEM images of glassy carbon microspheres: (A) shows the non-modified microspheres, and (B) and (C) show the microspheres with a Pd shell. Reproduced from ref. 50 with permission, © American Chemical Society 2007.

electrode surface makes them diffusionally accessible to a greater region of the solution on a short experimental timescale.

It is useful to compare experimental data with the theory discussed above. Consider the electrocatalytic reduction of protons at a palladium particle modified electrode:



Fig. 19 shows SEM images of glassy carbon microspheres before and after modification with Pd nanoparticles. The Pd nanoparticles are shown to be approximately spherical in shape. Fig. 20 shows a range of experimentally recorded voltammograms using this system. When  $\Theta = 0.445$  the diffusion layers overlap extensively and category 4 behaviour is observed for all scan rates studied. Accordingly, the voltammograms are peak shaped and the Randles–Ševčík equation is obeyed. When  $\Theta = 0.118$ , category 4 behaviour is observed in the limit of low scan rates while category 2 behaviour is observed in the limit of high scan rates.

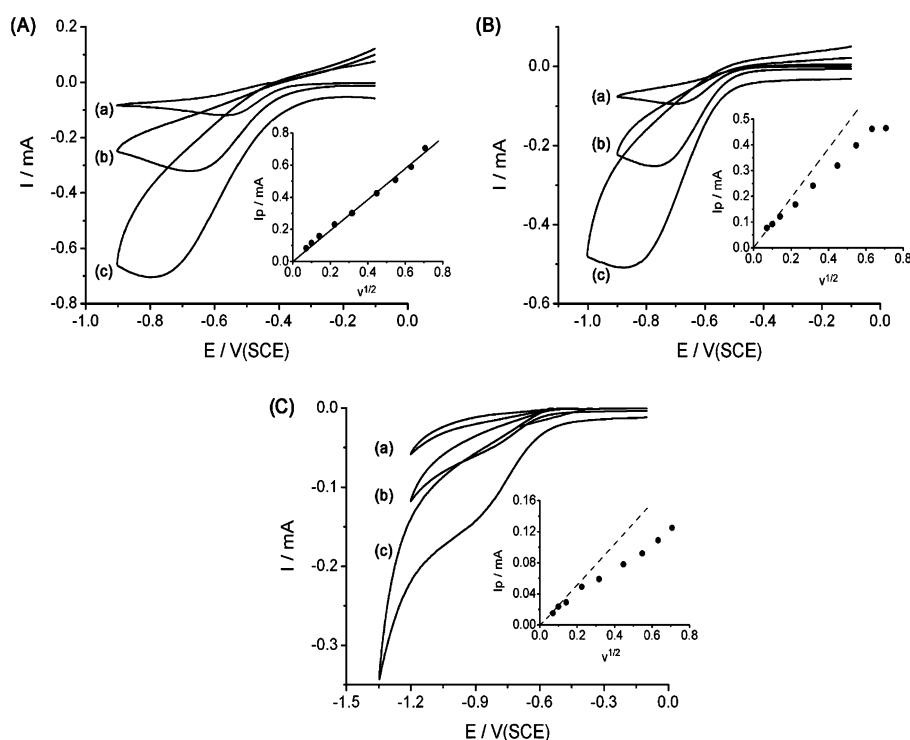
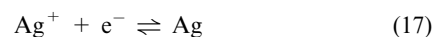


**Fig. 20** Cyclic voltammetry in 3 mM HCl, 0.1 M KCl at a 5 mm diameter BPPG electrode modified by the abrasive attachment of different amounts of Pd-CMs (palladium-carbon microspheres). The fractional surface coverage of particles is (A) 0.445, (B) 0.118, and (C)  $7.6 \times 10^{-3}$ . For each graph curves (a), (b), and (c) correspond respectively to voltammograms recorded at 10, 100, and 500  $\text{mV s}^{-1}$ . Reproduced from ref. 50 with permission, © American Chemical Society 2007.

The Randles–Ševčík equation is obeyed in the limit of low scan rates while at high scan rates, the peak current is invariant with scan-rate corresponding to steady-state voltammetry in the category 2 region. When  $\Theta = 7.6 \times 10^{-3}$ , category 4 behaviour is observed in the limit of low scan rates while category 2 behaviour is observed at intermediate scan rates and category 1 behaviour is observed at high scan rates. The Randles–Ševčík equation is obeyed in the limit of low scan rates while at intermediate scan rates, the peak current is invariant with scan-rate corresponding to steady-state voltammetry in the category 2 region. At very high scan rates, category 1 behaviour occurs and the Randles–Ševčík equation is obeyed: albeit multiplied by the factor  $4\Theta$  in order to account for the fact that diffusion occurs to each nanoparticle individually rather than towards the entire array.<sup>24</sup>

Fig. 21 shows a comparison between the peak current (normalised by the number of nanoparticles in the array) for experiment and simulation for a range of fractional surface coverages. As the fractional surface coverage decreases, the region of solution available to each nanoparticle increases leading to a larger relative current. In the limit of very low surface coverages, a steady-state response is attained, corresponding to the category 2 region.

A similar model to that considered above can be applied to stripping voltammetry. Ward-Jones *et al.*<sup>25</sup> have studied the reversible stripping reaction shown in eqn (17) at a random array of AgNPs:



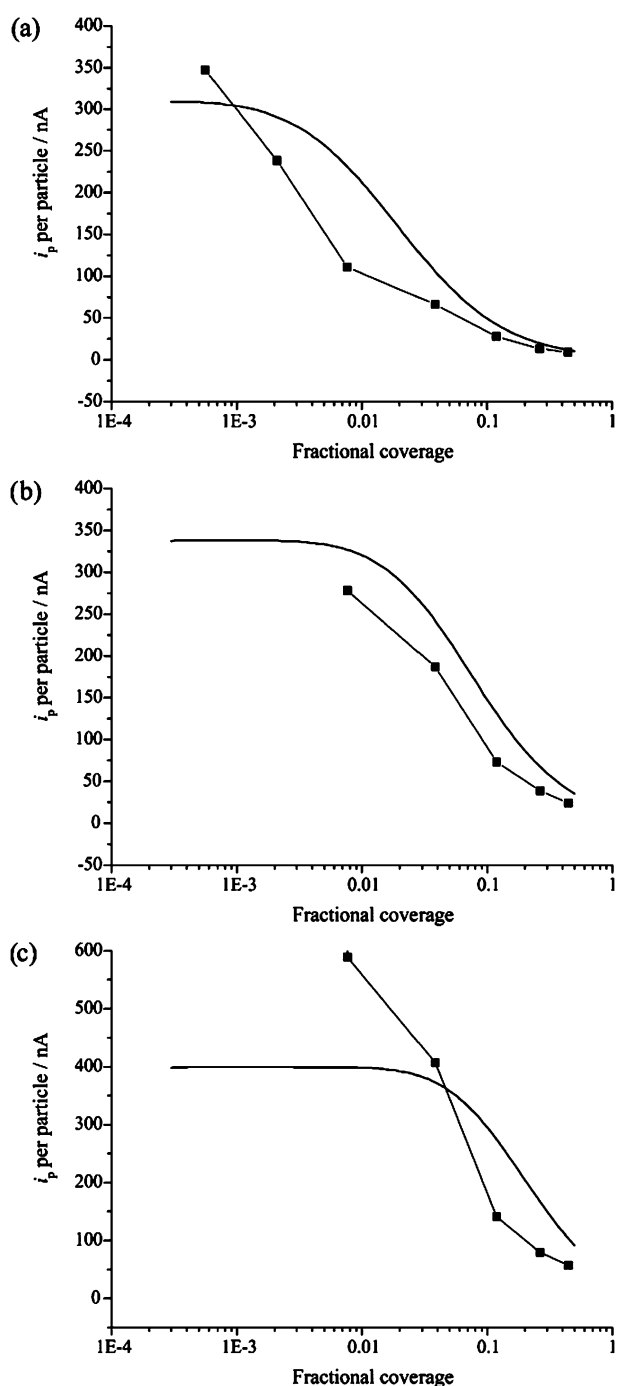


**Fig. 21** Variation of linear sweep peak height per particle with surface coverage of particles. Scan rates: (a)  $0.01$ , (b)  $0.1$ , (c)  $0.5 \text{ V s}^{-1}$ . Simulated data is shown by a solid line; experimental data is shown by connected squares. Reproduced from ref. 50 with permission, © American Chemical Society 2007.

The stripping voltammetry for different surface coverages is shown in Fig. 22. When the nanoparticles are of equal size, the stripping charge,  $Q$ , (measured by integrating the area under the voltammogram) is directly proportional to the nanoparticle surface coverage. Fig. 23 shows plots of  $E_p$  as a function of stripping charge. It can be seen that the peak potential becomes more positive as the stripping charge

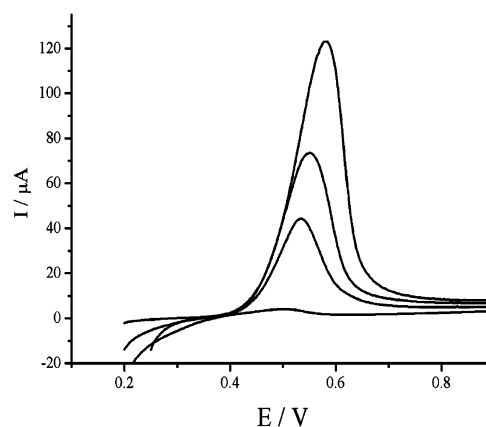


**Fig. 22** Stripping voltammetry for four different loadings of 80–120 nm diameter nanoparticles stripped into a  $0.1 \text{ M NaClO}_4$  solution at a scan rate of  $\sigma = 20 \text{ mV s}^{-1}$ . Reproduced from ref. 25 with permission, © American Chemical Society 2008.

(hence surface coverage) becomes higher. The diffusion layers are derived from  $\text{Ag}^+$  moving away from the surface during stripping. The diffusion layers overlap leading to category 1–4 behaviour as explained above. As the surface coverage increases, the diffusion layers overlap to a greater extent and hinder the diffusion of  $\text{Ag}^+$  from the surface. This leads to the effect of rate determining mass transport (and hence the voltammetric peak) being offset to more positive potentials.

## 5. Porosity effects: a caveat

The above discussion has assumed that the nanoparticles on the electrode surface are present at monolayer coverage or less. In some applications, especially electroanalysis,<sup>1,6</sup> thicker layers of nanoparticles may be used, so forming a porous layer on the electrode surface. This quantitatively changes the mass transport characteristics at the interface.

For a thick ( $>$  monolayer) modifying layer, the electrode surface can be thought of as a porous layer in which products in solution<sup>26</sup> are transported in between multiple layers of nanoparticles. The electrolysis of species within the porous layer can be approximately described using a model of a thin-layer cell of high electrode area (much higher than the area of the modifying supporting electrode) reflecting the large surface area of the nanoparticles within the porous layer. This contrasts with electrolysis at the corresponding 'naked' (unmodified) electrode where semi-infinite planar diffusion is the appropriate transport model. Fig. 24 shows comparative voltammograms simulated using the two models using a standard electrochemical rate constant of  $k_0 = 10^{-4} \text{ cm s}^{-1}$ , a diffusion coefficient of  $10^{-5} \text{ cm}^2 \text{ s}^{-1}$  and scan rate of  $100 \text{ mV s}^{-1}$  and assuming that the surface area of the nanoparticles is 30 times that of the naked electrode. Butler–Volmer kinetics is also assumed. Note that the thin layer model predicts a smaller peak to peak separation than the semi-infinite diffusion model and that the peaks appear with a larger overpotential in the latter model. It is evident that if the current measured at a nanoparticle modified electrode

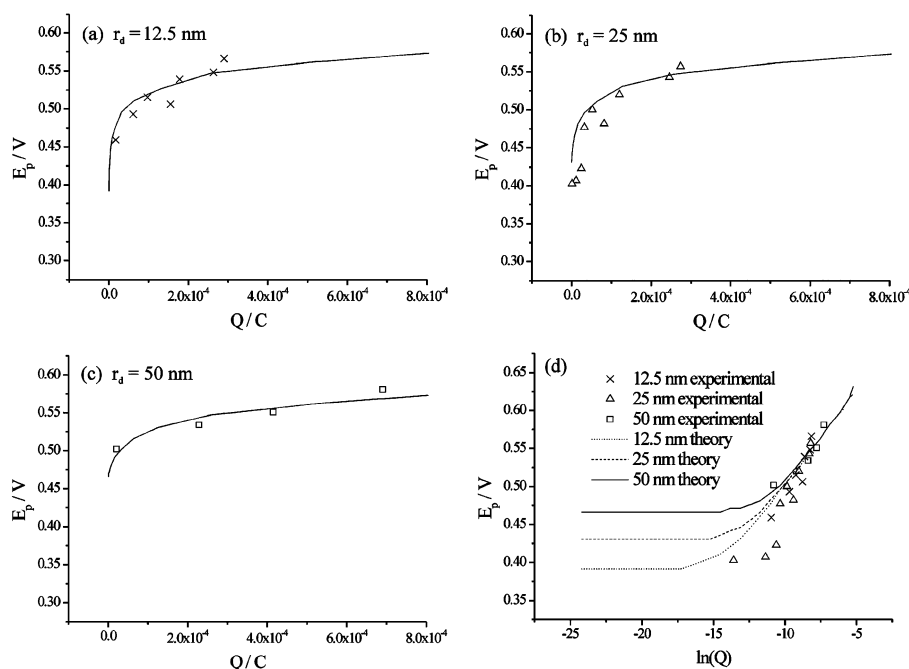


**Fig. 23** Plots of peak potential,  $E_p$ , measured experimentally (symbols) and predicted by a computational model (solid line) against the stripping charge,  $Q$ . Nanoparticle radius ( $r_{np}$ ): (a) 12.5 nm (sample 1), (b) 25 nm (sample 2), and (c) 50 nm (sample 3). (d) Same data plotted against  $\ln(Q)$ . In all cases, the scan rate,  $\sigma$ , is  $0.02 \text{ V s}^{-1}$ . Reproduced from ref. 25 with permission, © American Chemical Society 2008.

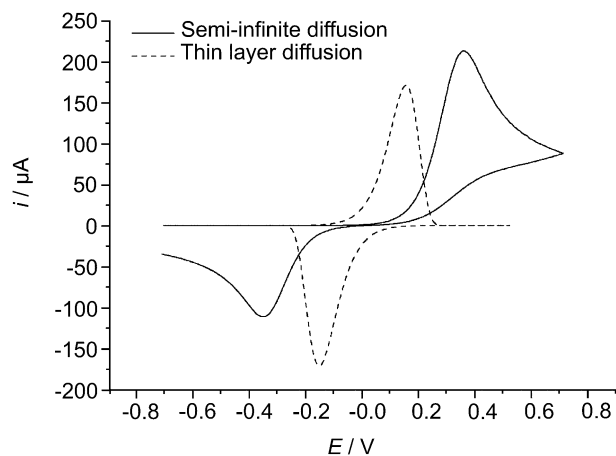


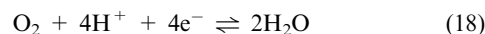
**Fig. 24** Comparison of linear sweep voltammetry using a semi-infinite and thin layer planar diffusion models. For both models,  $k_0 = 10^{-4} \text{ cm s}^{-1}$ ;  $D = 10^{-5} \text{ cm}^2 \text{ s}^{-1}$ ;  $\sigma = 0.1 \text{ V s}^{-1}$ ;  $c = 10^{-6} \text{ mol cm}^{-3}$ . Semi-infinite diffusion electrode area,  $A = 1 \text{ cm}^2$ ; thin layer area,  $A = 30 \text{ cm}^2$ ; thickness,  $l = 1 \text{ μm}$ . Reproduced from ref. 26 with permission, © Elsevier 2008.

has a significant contribution from a porous layer then the impression of an erroneously large electrochemical rate constant may be inferred. That is, a porous layer can give the false impression of speeding up an electrode process whereas in fact it is simply reducing the diffusional overpotential.

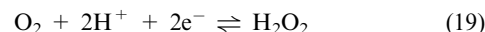
Porosity effects have been shown to operate in electrodes modified with thick layers of carbon nanotubes<sup>26–29</sup> and of  $\text{C}_{60}$ .<sup>30,31</sup> They are also likely to exist in some or even many electrodes modified with thick layers of metallic nanoparticles.

## 6. Changed electrode kinetics and mechanisms at the nanoscale

Earlier in this article we suggested that the changed electronic structure and adsorption behaviour at the nanoscale might induce changes of electrolytic reaction mechanism and kinetics. Thus, for example, gold atomic clusters ( $\text{Au}_n$ ;  $5 \leq n \leq 13$ ) stabilised by surfactants can reduce oxygen to water:<sup>32,33</sup>

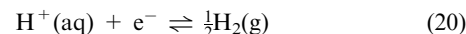


whereas at bulk gold a two electron process is seen:



In the above example a double electrode (ring-disc) was used to identify the presence or absence of  $\text{H}_2\text{O}_2$  generated on a disc electrode covered with electrodeposited layers of the nanomaterial.

In other work sub-monolayers of larger nanoparticles have been employed.<sup>34</sup> Thus the hydrogen evolution reaction:



carried out using either a silver macroelectrode or an array of silver nanoparticles showed very different Butler–Volmer kinetics as reported in Table 1: where  $\alpha$  is the transfer coefficient and  $k_0$  is the standard electrochemical rate constant.

**Table 1** Kinetic data for hydrogen evolution at silver

	$\alpha$	$k_0$
Macro silver	0.36	$6 \times 10^{-12} \text{ cm s}^{-1}$
Silver nanoparticles	0.16	$1 \times 10^{-6} \text{ cm s}^{-1}$

Important in this work was the correction for mass transport effects as described elsewhere in this article. Similarly the reaction of 4-nitrophenol<sup>35</sup> in aqueous solution was shown to have a quite different mechanism between a silver macro-electrode and arrays of 15–50 nm order nanoparticles. In the former case an  $\alpha$  value close to unity supported the possibility of the fast formation of the radical anion followed by a rate-determining chemical step, whereas for the nanoparticles a low  $\alpha$  value suggested slow, rate-determining electrode kinetics.

## 7. Modelling the behaviour of small (< 10 nm) nanoparticles

The Debye length, the distance over which electric fields are effectively screened in an electrolytic solution, ranges between 1 and 10 nm in aqueous solution for typical concentrations of electrolyte from 1 to 100 mM. The longer part of the range ( $r_D \approx 10$  nm) corresponds to weakly or self-supported solutions, as may be of interest in, for instance, biological applications. For electrodes with dimensions which approach this size, electric fields and migration effects strongly influence behaviour close to the electroactive surface, especially when the concentration of supporting electrolyte is small. Therefore, the study of electrolysis at small nanoparticles no longer admits some common assumptions such as electroneutrality, but rather requires a more thorough theoretical treatment. A range of 'non-classical' effects have been identified.

In consideration of the diffuse double layer, which at steady state compensates the excess charge on a nanoelectrode, recent work has shown that the effect of curvature on the double layer at a nanoparticle with radius less than or close to the solution Debye length causes deviation from the classical Gouy–Chapman theory,<sup>36,37</sup> for both hemispherical and cylindrical geometries. In particular, elevated and increasingly potential independent diffuse double layer capacitance is predicted, together with increased electric field at the nanoparticle surface and hence reduced ohmic drop at the plane of electron transfer. Since the Debye length is inversely dependent on ionic strength, these effects ought to occur at larger nanoparticles under conditions of low electrolytic support.

Size effects are equally important under conditions of dynamic electrolysis, such as in a voltammetric experiment with a potential step or potential sweep. Since the dimensions of the electrode, and hence the plane of electron transfer, are of the same order as the Debye length, the double layer and diffusion layer are entangled in a complex manner close to the electrode surface. The overall behaviour is not yet well understood, but it is safe to say that any attempt to model electrolysis at small nanoparticles must explicitly consider double layer structure. For instance, in a study of weakly supported chronoamperometry, Streeter *et al.* demonstrated that the decoupling of ohmic drop and double layer capacitance by a zero-field approximation is invalid at nanoelectrodes;<sup>38</sup> by contrast, this approximation has been successfully applied to fit experimental data for weakly supported voltammetry at larger electrodes.<sup>39,40</sup> Yang *et al.* and Liu *et al.* have considered some features of the influence of the double layer on voltammetry at nanoelectrodes.<sup>41,42</sup>

Furthermore, the magnitudes of charge and distance associated with small nanoparticles render continuum theories altogether inappropriate under many circumstances. For example, a 5 nm particle with a mean surface capacitance of  $10 \mu\text{F cm}^{-2}$  will have an excess charge of fewer than 50 electrons at a 200 mV overpotential away from the potential of zero charge. For such small excess charges, components of the electron conduction bands may be observably discrete, and the charging process is therefore quantised. The tunnelling of single electrons to and from discrete wavefunctions within the nanoparticle may be measured, with charging occurring one electron at a time in a so-called 'Coulomb staircase'<sup>43–45</sup> – alkanethiol-modified Au nanoparticles have been the most popular systems for experimental investigation to date. Classical interpretations of capacitance clearly do not apply here; any theoretical treatment which ignores quantisation will exclude experimentally significant effects.

Finite molecule or ion volume effects may equally become significant at a small nanoparticle scale. Traditional mean field (continuum) theories cease to be reliable at very short length scales, and a fuller consideration of finite volume effects leads to a revised understanding of double layer structure. López-García *et al.* have considered this topic most completely using a simulation method based on the modified Poisson–Boltzmann equation;<sup>46</sup> the references therein represent an adequate review of the prior literature.

Similarly, the assumption of a continuous solvent is weaker, since the surface structure of the nanoparticle controls the local orientation of solvent molecules, and the number of solvent molecules making up the compact double layer is not sufficiently large to treat solution as continuous approaching the surface. Especially in consideration of the close coupling of the double layer to the diffusion layer, such effects may influence experimental observations for voltammetry or impedance spectroscopy experiments. The magnitude of such effects has not yet been thoroughly investigated in an electrochemical context, although some studies have used molecular dynamics to investigate the limitations of mean field theories<sup>47–49</sup> for describing the electrical double layer. The fuller analysis of charge dynamics and electrolysis at the nanoscale remains in its infancy, however.

## 8. Conclusion

It has been shown that, in almost all cases, the voltammetric response from a nanoparticle-modified electrode is substantially different from that expected from a macroelectrode. Discrepancies occur due to a combination of electrode kinetics and mass transport. Using computer simulations, it is possible to deconvolute these factors and obtain useful experimental information regarding the nanoparticle specific effects.

## References

- 1 C. M. Welch and R. G. Compton, *Anal. Bioanal. Chem.*, 2006, **384**, 601–619.
- 2 G. J. Hutchings, *Chem. Commun.*, 2008, 1148–1164.
- 3 M. D. Hughes, Y.-J. Xu, P. Jenkins, P. McMorn, P. Landon, D. I. Enache, A. F. Carley, G. A. Attard, G. J. Hutchings, F. King,



- E. H. Stitt, P. Johnston, K. Griffin and C. J. Kiely, *Nature*, 2005, **437**, 1132–1135.
- 4 A. C. Templeton, W. P. Wuelfing and R. W. Murray, *Acc. Chem. Res.*, 2000, **33**, 27–36.
- 5 R. W. Murray, *Electroanal. Chem.*, 1984, **13**, 191–368.
- 6 F. W. Campbell and R. G. Compton, *Anal. Bioanal. Chem.*, 2010, **396**, 241–259.
- 7 A. O. Simm, X. Ji, C. E. Banks, M. E. Hyde and R. G. Compton, *ChemPhysChem*, 2006, **7**, 704–709.
- 8 F. W. Campbell, S. R. Belding, R. Baron, L. Xiao and R. G. Compton, *J. Phys. Chem. C*, 2009, **113**, 9053–9062.
- 9 H. Taube, *Angew. Chem., Int. Ed. Engl.*, 1984, **23**, 329–339.
- 10 M. J. Weaver and F. C. Anson, *Inorg. Chem.*, 1976, **15**, 1871–81.
- 11 B. W. Mao, Z. Q. Tian and M. Fleischmann, *Electrochim. Acta*, 1992, **37**, 1767–1770.
- 12 J. X. Wang, R. R. Adzic, O. M. Magnussen and B. M. Ocko, *Surf. Sci.*, 1995, **344**, 111–121.
- 13 F. W. Campbell, Y.-G. Zhou and R. G. Compton, *New J. Chem.*, 2010, **34**, 187–189.
- 14 F. W. Campbell and R. G. Compton, *Int. J. Electrochem. Sci.*, 2010, **5**, 407–413.
- 15 C. Batchelor-McAuley, G. G. Wildgoose and R. G. Compton, *New J. Chem.*, 2008, **32**, 941–946.
- 16 G. Flätgen, S. Wasle, M. Lübke, C. Eickes, G. Radhakrishnan, K. Doblhofer and G. Ertl, *Electrochim. Acta*, 1999, **44**, 4499–4506.
- 17 I. Streeter and R. G. Compton, *J. Phys. Chem. C*, 2007, **111**, 18049–18054.
- 18 T. J. Davies, B. A. Brookes, A. C. Fisher, K. Yunus, S. J. Wilkins, P. R. Greene, J. D. Wadhawan and R. G. Compton, *J. Phys. Chem. B*, 2003, **107**, 6431–6444.
- 19 B. A. Brookes, T. J. Davies, A. C. Fisher, R. G. Evans, S. J. Wilkins, K. Yunus, J. D. Wadhawan and R. G. Compton, *J. Phys. Chem. B*, 2003, **107**, 1616–1627.
- 20 T. J. Davies, S. Ward-Jones, C. E. Banks, J. Del Campo, R. Mas, F. X. Munoz and R. G. Compton, *J. Electroanal. Chem.*, 2005, **585**, 51–62.
- 21 T. J. Davies and R. G. Compton, *J. Electroanal. Chem.*, 2005, **585**, 63–82.
- 22 T. J. Davies, C. E. Banks and R. G. Compton, *J. Solid State Electrochem.*, 2005, **9**, 797–808.
- 23 S. R. Belding, E. J. F. Dickinson and R. G. Compton, *J. Phys. Chem. C*, 2009, **113**, 11149–11156.
- 24 S. R. Belding and R. G. Compton, *J. Phys. Chem. C*, 2010, **114**, 8309–8319.
- 25 S. E. Ward Jones, F. W. Campbell, R. Baron, L. Xiao and R. G. Compton, *J. Phys. Chem. C*, 2008, **112**, 17820–17827.
- 26 I. Streeter, G. G. Wildgoose, L. Shao and R. G. Compton, *Sens. Actuators, B*, 2008, **133**, 462–466.
- 27 D. Menshykau and R. G. Compton, *Electroanalysis*, 2008, **20**, 2387–2394.
- 28 M. J. Sims, N. V. Rees, E. J. F. Dickinson and R. G. Compton, *Sens. Actuators, B*, 2010, **144**, 153–158.
- 29 G. P. Keeley and M. E. G. Lyons, *Int. J. Electrochem. Sci.*, 2009, **4**, 794–809.
- 30 L. Xiao, G. G. Wildgoose and R. G. Compton, *Sens. Actuators, B*, 2009, **138**, 524–531.
- 31 L. Xiao, G. G. Wildgoose, A. Crossley and R. G. Compton, *Sens. Actuators, B*, 2009, **138**, 397–401.
- 32 M. J. Rodriguez-Vázquez, M. C. Blanco, R. Lourido, C. Vázquez-Vázquez, E. Pastor, G. A. Planes, J. Rivas and M. A. López-Quintela, *Langmuir*, 2008, **24**, 12690–12694.
- 33 C. Jeyabharathi, S. S. Kumar, G. V. M. Kiruthika and K. L. N. Phani, *Angew. Chem., Int. Ed.*, 2010, **49**, 2925–2928.
- 34 F. W. Campbell, S. R. Belding, R. Baron, L. Xiao and R. G. Compton, *J. Phys. Chem. C*, 2009, **113**, 14852–14857.
- 35 F. W. Campbell, S. R. Belding and R. G. Compton, *ChemPhysChem*, 2010, DOI: 10.1002/cphc.200900863.
- 36 E. J. F. Dickinson, J. G. Limon-Petersen, N. V. Rees and R. G. Compton, *J. Phys. Chem. C*, 2009, **113**, 11157–11171.
- 37 M. C. Henstridge, E. J. F. Dickinson and R. G. Compton, *Chem. Phys. Lett.*, 2010, **485**, 167–170.
- 38 I. Streeter and R. G. Compton, *J. Phys. Chem. C*, 2008, **112**, 13716–13728.
- 39 E. J. F. Dickinson and R. G. Compton, *J. Phys. Chem. C*, 2009, **113**, 17585–17589.
- 40 J. G. Limon-Petersen, J. T. Han, N. V. Rees, E. J. F. Dickinson, I. Streeter and R. G. Compton, *J. Phys. Chem. C*, 2010, **114**, 2227–2236.
- 41 Y. Liu, R. He, Q. Zhang and S. Chen, *J. Phys. Chem. C*, 2010, **114**, 10812–10822.
- 42 X. Yang and G. Zhang, *Nanotechnology*, 2007, **18**, 335201.
- 43 S. Chen, R. S. Ingrma, M. J. Hostetler, J. J. Pietron, R. W. Murray, T. G. Schaaff, J. T. Khoury, M. M. Alvarez and R. L. Whetten, *Science*, 1998, **280**, 2098–2101.
- 44 H. Graf, J. Vancea and H. Hoffmann, *Appl. Phys. Lett.*, 2002, **80**, 1264–1266.
- 45 R. Negishi, T. Hasegawa, H. Tanaka, K. Terabe, H. Ozawa, T. Ogawa and M. Aono, *Surf. Sci.*, 2007, **601**, 3907–3911.
- 46 J. J. López-García, M. J. Aranda-Rascón and J. Horno, *J. Colloid Interface Sci.*, 2007, **316**, 196–201.
- 47 E. Spohr, *Solid State Ionics*, 2002, **150**, 1–12.
- 48 F. Grün, M. Jardat, P. Turq and C. Amatore, *J. Chem. Phys.*, 2004, **120**, 9648–9655.
- 49 R. J. White and H. S. White, *Langmuir*, 2008, **24**, 2850–2855.
- 50 I. Streeter, R. Baron and R. G. Compton, *J. Phys. Chem. C*, 2007, **111**, 17008–17014.